



*Theory article*

# **Analysis of the nonlinear dynamic behavior of longitudinal systems in heavy-haul trains**

**Leiting Wang<sup>1</sup>, Yang Jin<sup>2</sup>, Wangxiang Li<sup>1,\*</sup> and Chenyang Tang<sup>1</sup>**

<sup>1</sup> School of Mechanical Engineering, Lanzhou Jiaotong University, Lanzhou 730070, China

<sup>2</sup> National Key Laboratory of Rail Transit Carrying Systems, Southwest Jiaotong University, Chengdu 610031, China

\* **Correspondence:** Email: wanxiangli@mail.lzjtu.cn.

**Abstract:** The payload, coupler slack, and buffer device performance in heavy-haul trains substantially affect their longitudinal dynamic systems under operational conditions. These factors result in the bifurcation of the system, consequently leading to chaos. To study this phenomenon in depth, a two-degrees-of-freedom longitudinal dynamics model of the train is established. The system is analyzed using the fourth-order Runge–Kutta (R-K\_4) numerical integration method, incorporating bifurcation diagrams, phase planes, Poincaré mapping, and time-domain analysis to elucidate the trajectory of the system as it transitions into a chaotic state of motion via period-doubling bifurcations and quasi-periodic motions. A comprehensive analysis of the complex nonlinear dynamics of the train's longitudinal system can establish a theoretical foundation for forecasting and regulating the chaotic motion of the train system.

**Keywords:** heavy-haul trains; coupler buffer device; periodic motion; bifurcation; chaos

---

## **1. Introduction**

The strategy employed by heavy-haul trains to augment freight capacity mostly involves extending the length of the train formation and increasing the load; nevertheless, this approach results in elevated axle weight and longitudinal force [1]. The augmentation of a train's longitudinal force would directly influence the smoothness and safety of the vehicle's operation, indicating that the technological advancement of heavy-haul trains is intricately linked to the study of trains' longitudinal

dynamics. A train has multiple vehicles linked by coupler buffer devices. The buffer device serves as a spring damping mechanism and plays a crucial role in absorbing impact energy; the stability of the train's longitudinal dynamics is significantly reliant on the coupler buffer system.

The longitudinal dynamics system of heavy-haul trains contains several nonlinear factors, typically the main coupler's slack, the nonlinear impedance characteristics of the buffer, and the nonlinear operating characteristics of traction and braking. Currently, the nonlinear characterization of heavy-haul train systems has mainly focused on fault diagnosis [2–4], coupler strength analysis [5,6], fatigue life studies [7–9], and mathematical modeling of buffer devices [10–15]. Although different models of buffer devices have different structural and material properties and different mathematical models have been constructed, the hysteresis phenomenon exists in friction-type buffer devices. To address the hysteresis phenomenon of buffer devices, Yang et al. [16] used a hysteresis coupler force model based on regularized velocity, Zhang et al. [17] used a segmented nonlinear function to fit the hysteresis curve of the coupler force versus displacement, and Liu [18] and Yang et al. [19] utilized a slant wedge spring model using the look-up table method to construct the hysteresis curve of the buffer device. The couplers used in heavy-haul trains have a connecting slack, where collisions and dry friction are often associated with the phenomenon. Therefore, the effects of the coupler slack and dry friction on the longitudinal dynamics of the train are getting more and more attention, among which some research [1] has fully considered the effects of the internal and linkage slack of the couplers, as well as the friction at the couplers' contact points on the impact acceleration of the system. The polynomial exponential fitting model proposed by Ward and Leonard [20] fits the dry friction of friction-type coupler buffer devices well. Zhang et al. [21] incorporated the role of the friction on the coupler's tail arc surface on the coupler's deflection angle in the model, whereby the effect of this factor on the axle's transverse system was explored. Wu et al. [22] comprehensively considered the effect of friction between the coupler head and the friction pair on the coupler's inclination angle and then analyzed the stability of the train's operation.

In the mechanical power system, with a change in the nonlinear factors, the system may have nonlinear dynamic characteristics such as doubling bifurcation, Hopf bifurcation, and grazing bifurcation, showing periodic oscillation, quasi-periodic oscillation, and chaos [23,24]. Numerous nonlinear elements inside the heavy-haul train system can induce diverse characteristics in the system's solutions, including crisis, which will appear in the form of bifurcation and chaos. On the basis of the current research results of bifurcation and chaos in collision systems with slacks, some scholars have begun to explore the influence of coupler buffers on train systems from the perspective of bifurcation and chaos. Popp and Stelzer [25] studied the path of a single-degree-of-freedom dry friction oscillator to periodic bifurcation and chaos under harmonic excitation. Lv et al. [26] discussed the transition between the single-impact periodic motion and the sliding bifurcation of a two-degrees-of-freedom collision system with slack. Yadav et al. [27,28], on the basis of the coupler buffer system of the Association of American Railroads train, studied the influence of the coupler's inertia, slack, and dry friction on the longitudinal dynamics of trains.

In this paper, a kind of heavy-haul train coupler and an MT-2 buffer device commonly used in China were selected as the research objects. On the basis of existing research, a mathematical model of the MT-2 friction buffer device with hysteresis characteristics was established. From the perspective of bifurcation and chaos, the influence of nonlinear factors on the longitudinal dynamic response of heavy-haul trains under straight-line operating conditions was explored. The path of the system from period-doubling and almost periodic motion to chaos through a phase-locked transition under

parameter changes was observed.

## 2. The two-degrees-of-freedom model of a heavy-haul train

The couplings between the carriages of the train are realized by coupler locking. A schematic diagram of the connection between carriages is shown in Figure 1(a); the structure of the coupler buffer device is shown in Figure 1(b).

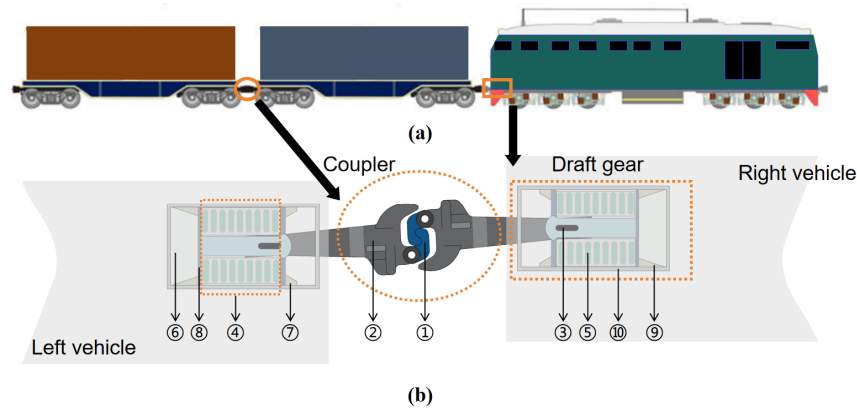


**Figure 1.** (a) Connection diagram of adjacent carriages. (b) Amplification diagram of a coupler buffer device. ① Knuckle pivot pin; ② coupler head; ③ draft sill; ④ spring; ⑤ impact seat; ⑥ striking casting; ⑦ front draft lug; ⑧ backboard; ⑨ rear draft lug; ⑩ draft sill.

Under the condition of locomotive traction or braking, the right coupler buffer device is subjected to the traction or braking force of the locomotive, and the force is transmitted to the left coupler (2) through the device (1) after buffering. The left coupler buffer device exhibits impedance characteristics under the action of this force, realizes buffering, reduces the impact of traction or braking force on the carriage, and realizes the stability of the train running in the longitudinal direction.

In addition to the rolling stock, the structure between the carriages of freight trains has obvious parameter symmetry. In studies, it is a common method to take two of the carriages for research. Therefore, according to the diagram of the train model in Figure 1, the left two carriages were selected as the research object, and the following physical model shown in Figure 2 was established.

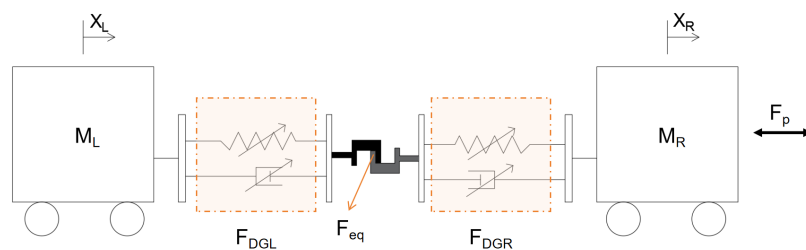


**Figure 2.** Physical model of the coupler buffer device.

In order to investigate the effect of the vehicle's longitudinal force on the system's response on a straight road section, the following equations for the longitudinal dynamics of the train are established according to

D'Alembert's law:

$$\begin{cases} M_L \frac{d^2 X_1}{dt^2} - F_{eq}(Y, \dot{Y}) - F_{DGL}(X_1, \dot{X}_1) - F_p(T) = 0 \\ M_R \frac{d^2 X_2}{dt^2} + F_{eq}(Y, \dot{Y}) + F_{DGR}(X_2, \dot{X}_2) - F_p(T) = 0 \end{cases}, \quad (1)$$

where  $F_p$  is the traction or braking force provided by the right-hand rolling stock (hereinafter referred to as the external excitation force),  $M_L$  is the equivalent mass of the left carriage and the coupler buffer device, and  $M_R$  is the equivalent mass of the right carriage and the coupler buffer device. The equivalent contact force at the coupler head is  $F_{eq}$ , and the longitudinal impedance forces of the buffer devices on the left and right sides are  $F_{DGL}$  and  $F_{DGR}$ , respectively.

The displacements of the right and left coupler buffer devices are  $X_2$  and  $X_1$ , respectively. Assuming that the rightward movement is positive, the relative displacement and relative velocity are:

$$\begin{cases} Y = X_1 - X_2 \\ \dot{Y} = \dot{X}_1 - \dot{X}_2 \end{cases}. \quad (2)$$

The traction force or braking force of the train under operation conditions is a random force, but this paper mainly discusses the influence of the structural characteristics of the coupler buffer device on the response of the longitudinal system of the train during the impact. Therefore, the harmonic excitation force is used as the external excitation of the system [28].

$$F_p = F_t \sin(\Omega t + \varphi) \quad (3)$$

### 2.1. Longitudinal equivalent contact force of the coupler

There are two main reasons for the existence of free slack in coupler crisis: structural needs and wear during use. There are three relative positions of the coupler heads and the knuckle pivot pins in the free slack, as shown in Figure 3.

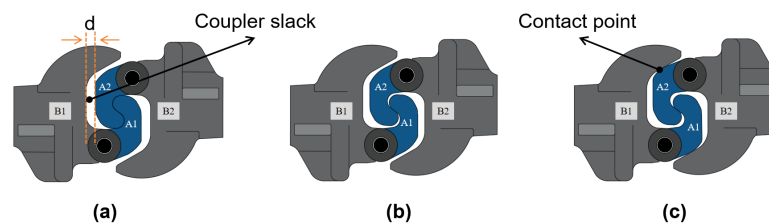


**Figure 3.** Relative position of coupler knuckles and the coupler heads.

When the relative position of the couplers is as shown in Figure 3(b), the couplers' state is free, and there is no significant force transfer in the longitudinal direction of the couplers. Therefore, the collision forces  $F_c = 0$ ,  $F_f = 0$  can be considered at this stage. Figure 3(c) states that the relative displacement between the coupler (B2) and the knuckle pivot pin (B1) is less than the complete clearance  $d$ , and the collision and friction occur between the coupler (B1) and the knuckle pivot pin (A2). At this time, the equivalent contact force at the coupler is  $F_{eq}$ :

$$F_{eq} = F_c + F_f, \quad (4)$$

where  $F_c$  and  $F_f$  are components in the longitudinal direction.

$$F_c = \begin{cases} \cos \psi (K_c \frac{Y-d}{\cos \psi} + C_c \dot{Y}) & Y \geq d \\ 0 & -d < Y < d. \\ \cos \psi (K_c \frac{Y+d}{\cos \psi} + C_c \dot{Y}) & Y \leq -d \end{cases} \quad (5)$$

The friction models mainly include the Coulomb model, the static–dynamic model, and the exponential model [29]. The friction model of the coupler generally adopts the Coulomb friction model [30]. Therefore, the formula for calculating the longitudinal component of the friction force is

$$F_f = \begin{cases} \mu_k (K_c \frac{Y-d}{\cos \psi} + C_c \dot{Y}) \sin \psi & Y \geq d, Y \leq -d \\ 0 & -d < Y < d \end{cases}. \quad (6)$$

In Eqs (5) and (6),  $K_c$  and  $C_c$  are the stiffness and damping of the coupler, respectively;  $\psi$  is the contact angle of the coupler, as shown in Figure 4. Assuming that  $R$  is the surface profile radius of the coupler, the contact angle can be calculated according to the relationship between the surface profile radius of the coupler and the coupler's slack:

$$\psi = \cos^{-1}[(R - d/R)]. \quad (7)$$

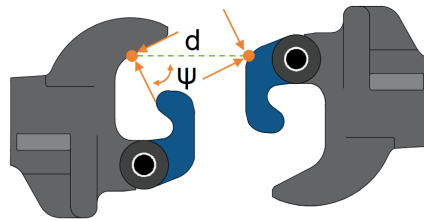


**Figure 4.** Contact angle between the coupler head and the knuckle pivot pin.

## 2.2. Buffer model

At present, there are three main modeling methods for the buffer devices, namely the ‘black box model’, the ‘gray box model’, and the ‘white box model’. In this paper, the black box model strategy is used to model the MT-2 buffer device by means of experimental data fitting. The experimental impact data of the buffer device are mainly from the literature [30]. After smoothing and denoising of the experimental data, the MT-2 buffer’s stroke and impedance characteristic curves under the initial impact velocity of 3–9 km/h were obtained, as shown in Figure 5(a). The characteristic curves of the buffer device under different initial impact velocities were fitted. Referring to the modeling method of Hsu and Peters [31], and Cole et al. [32] for the buffer device, a polynomial exponential fitting model was constructed, as shown in Eq (8). The mathematical model was simulated and verified, and the hysteresis curves thus obtained were compared with the original impedance characteristic curves, as shown in Figure 5(b)–(h). According to the comparison diagrams, the simulation model can reproduce the impedance characteristics of the buffer, and it shows excellent consistency with the actual impedance characteristic curves of the buffer device, so the model has certain rationality and accuracy.

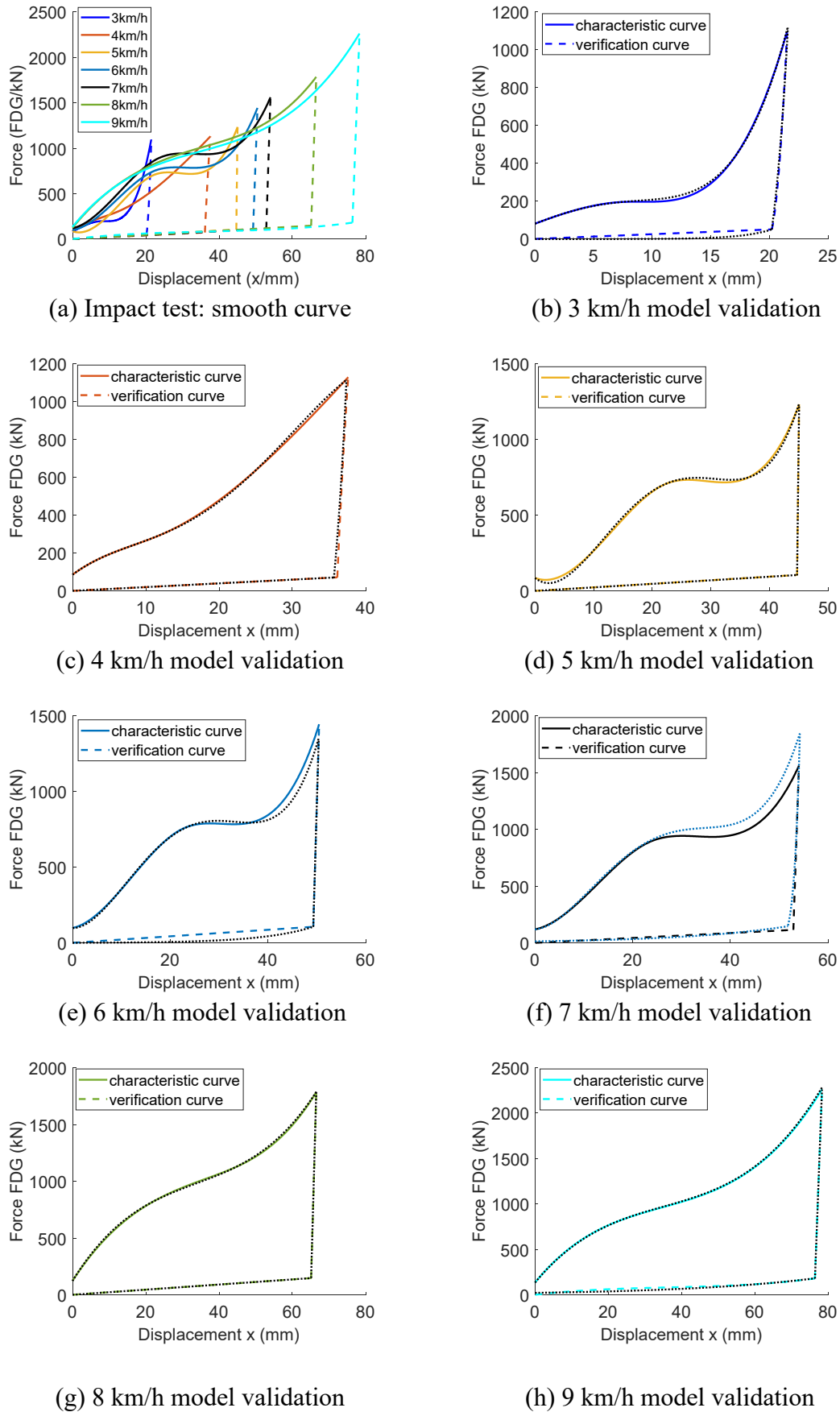


**Figure 5.** Force–displacement characteristic curves.

The characteristic curve of the buffer device at different impact velocities satisfies the following polynomial mathematical model:

$$F_{DG} = F_0 + F_1 e^{\gamma_1 X_1} + F_2 e^{\gamma_2 X_1} + F_3 + F_4 \left| \frac{X_1}{x_{max}} \right|^p \cdot \exp \left( -\gamma_3 \cdot \left| \frac{\dot{X}_1}{\dot{x}_{max}} \right|^r \right) \quad (8)$$

where  $F_0, F_1, F_2, \gamma_1, \gamma_2$  are the tuning parameters of the static components; and  $F_4, p, \gamma_3, x_{max}, \dot{x}_{max}$  are the tuning parameters of the dynamic components. These tuning parameters are determined by fitting the force–displacement characteristic curves of the buffer device using a curve fitting tool. In this paper, the coupler buffer system model established when the initial impact velocity is 7 km/h is selected as the main research object, and some tuning parameters thus obtained are shown in Table 1.

**Table 1.** Fitting parameters of coupler buffer device.

Parameter	$\dot{Y} \geq 0$	$\dot{Y} < 0$
	$0 \leq Y < D$	$Y \geq D$
F0	$-3.6 \times 10^4$	$-2.699 \times 10^4$
F1	$3.6 \times 10^4$	$2.699 \times 10^4$
F2	0.0103	-0.2033
F4	$1.5 \times 10^4$	$1.2 \times 10^4$
$\gamma_1$	16.00	0.03279
$x_{max}$	0.20	0.20
p	1.12	1.45

The damping of the rigid impact system is generally Rayleigh-type proportional damping, and the instantaneous change in velocity before and after the collision should be determined by the recovery coefficient  $R$ . However, the mass matrix and stiffness matrix in this study do not satisfy the condition of orthogonality and do not belong to the category of Rayleigh proportional damping, so the collision coefficient is not considered. However, since  $F_{DGL}$  is considered to be the force transmitted to the left vehicle, the simulated acceleration can be calculated by the following equation:

$$\ddot{X}_1 = \frac{F_{DGL}}{2M_v}, \quad (9)$$

where  $M_v$  is the total weight of self-weight and load. Some parameters of the current heavy-haul trains in China are shown in Table 2.

**Table 2.** Parameters of heavy-haul trains.

Parameter	Symbol	Values
Train weight	$M_0(t)$	20
The effective mass of the coupler system	$M_L = M_R$ (kg)	415
Contact angle	$\cos\psi$	0.9775
Coupler's coupling clearance	d/mm	10

### 3. The path of the system to chaos through bifurcation

#### 3.1. The influence of excitation frequency on the system's response

Referring to the simulation results of the coupler force of heavy-haul trains in [33], this paper assumes that the initial state of the train is  $X_0 = [0.05; -0.05; 0.01; 0.05]$ , the amplitude of the external excitation force  $F_t = 5 \times 1e5$ , and the friction coefficient  $\mu = 0.2$ . The fixed-step fourth-order Runge–Kutta [34] numerical integration method is used to solve the impact vibration system. Taking the external excitation frequency  $\omega$  as the bifurcation parameter, the local bifurcation diagram of the system is as shown in Figure 6. In order to better reflect the response characteristics of the system, this study constructed Poincaré maps  $T$  of the periodic collision of the system, and analyzes the changes and existing areas of the periodic motion of the system.

$$T = \{(X_1, X_2, \dot{X}_1, \dot{X}_2, \tau) \in R^4 \times S, \tau = 0, X_1 - X_2 = d, \dot{X}_1 - \dot{X}_2 > 0\}. \quad (10)$$

In Figure 6,  $P$  represents the period of the process,  $1P$  represents the fundamental vibration, the period is  $T$ , and  $2^n P$  represents  $n$  times the period of the fundamental vibration ( $n = 0, 1, 2, \dots$ ) [35,36]. It can be seen from Figure 6 that when  $\omega \in [5.536, 5.654]$ , inverse doubling bifurcation occurs with a decrease in the excitation frequency of the system.

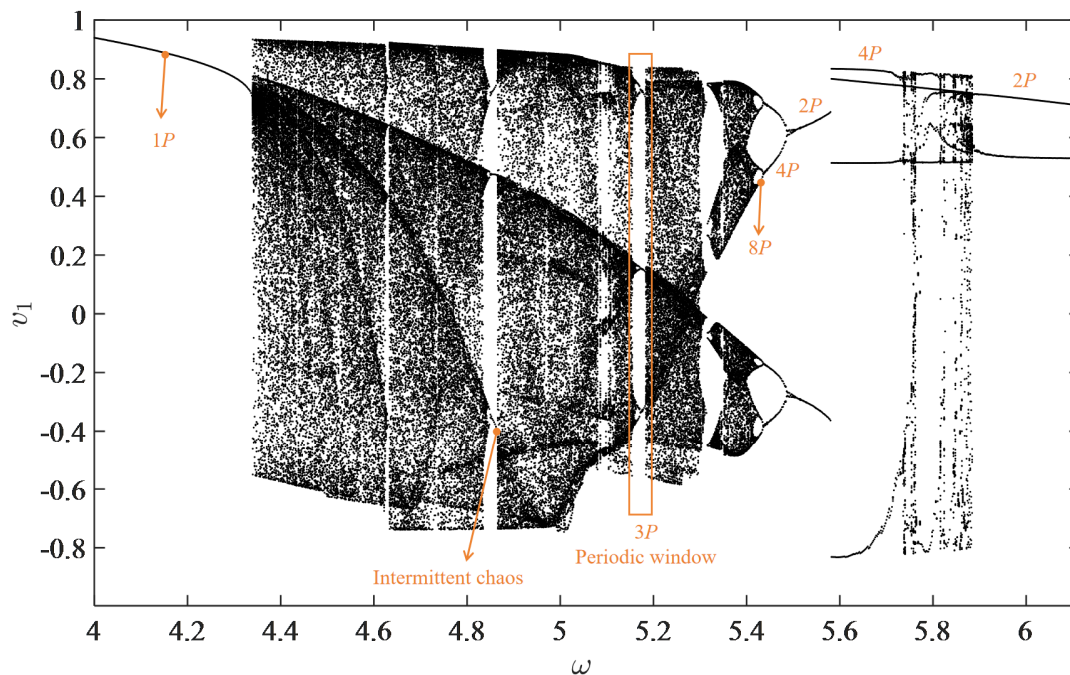


**Figure 6.** Bifurcation diagram ( $\omega \in [4, 5.5]$ ).

According to the Poincaré map in Figure 7(a), it can be seen that the system's motion is  $4P$  when  $\omega = 5.654$ . It can also be seen from Figure 8(a) that the phase plane oscillates due to the system's friction.

For the case when the excitation frequency is reduced to the crossing frequency  $\omega = 5.536$ , the Poincaré section diagram is shown in Figure 7(b). The system undergoes inverse doubling bifurcation. The stable fixed points of the Poincaré map of the system are reduced from 4 to 2, and the attractor

changes from Period 4 to Period 2. When  $\omega$  continues to decrease to  $\omega = 5.452$ , the number of stable fixed points of the system changes from 2 to 8 after two doubling bifurcations, and the 2-periodic attractor evolves into an 8-periodic attractor. As  $\omega$  continues to decrease, the system's instability briefly enters the chaotic state.

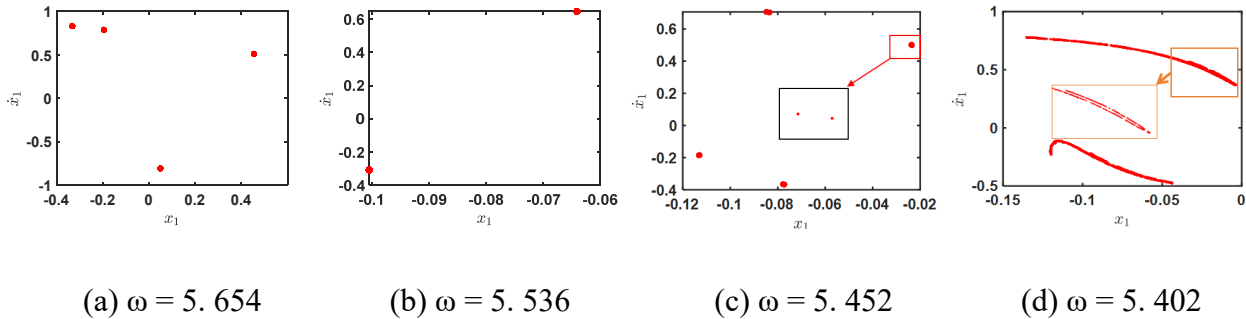


**Figure 7.** Poincaré maps.

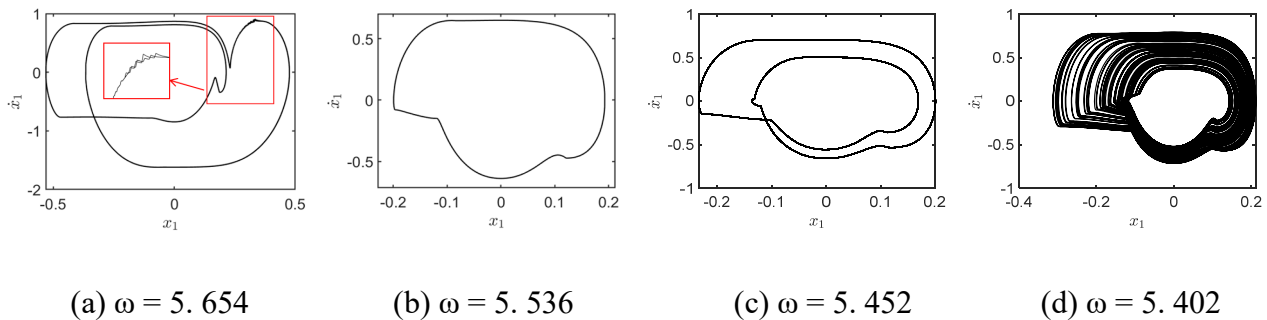


**Figure 8.** Phase plane diagrams.

When the excitation frequency continues to decrease to  $\omega = 5.18$ , the system enters the  $3P$  periodic window from the chaotic state, as it is shown in Figure 9(a). Then it is transformed into a  $6P$  state at  $\omega = 5.178$  and enters a chaotic state. According to the bifurcation diagram in Figure 6, it can be observed that the boundary crisis occurs at the excitation frequency  $\omega = 4.34$ , and the system transitions from an unstable chaotic state to a  $1P$  stable motion state.

From the changes in displacement and velocity in the phase diagrams above, it can be seen that there is a gradual change in velocity during the collision, i.e., the velocity of the coupler does not jump immediately when the collision occurs, and the impedance characteristics of the buffer will make the velocity undergo a gradual buffer response process after the impact force is applied. Due to the continuously applied external force  $F_P$ , the speed will gradually reverse. With a change in  $\omega$ , the system exhibits rich nonlinear dynamic characteristics.

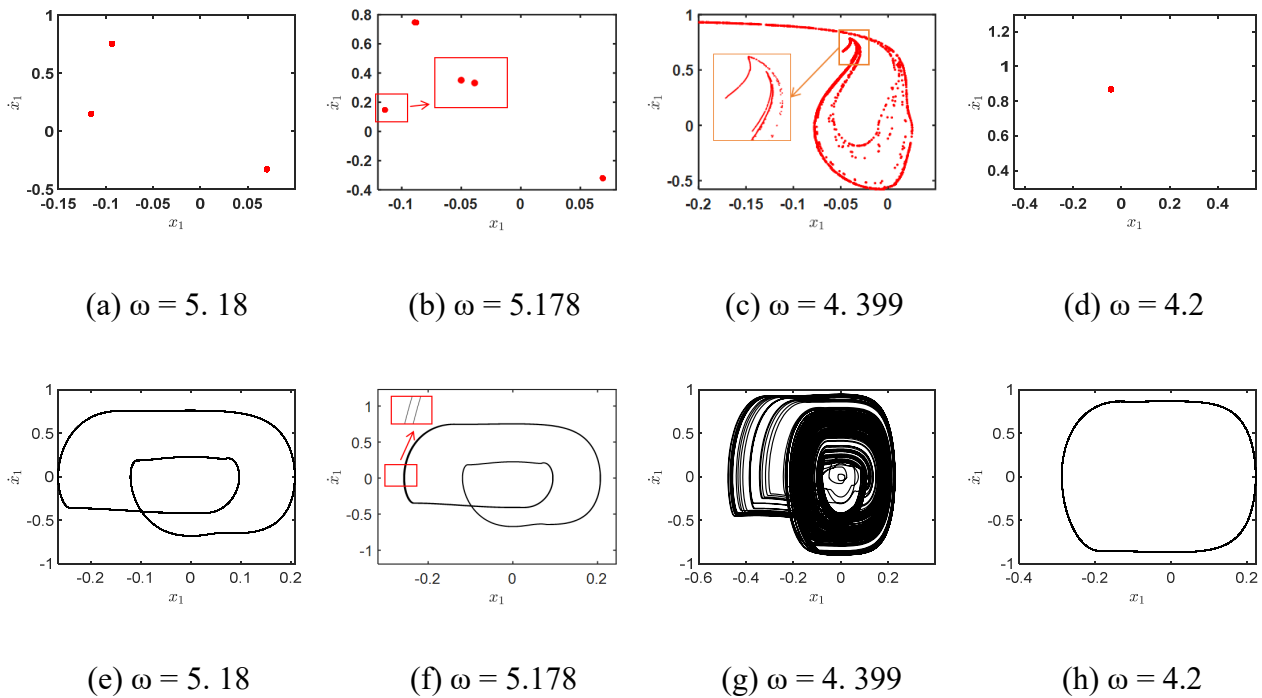


**Figure 9.** Poincaré maps (a)–(d); phase plane diagrams (e)–(h).

### 3.2. The influence of the amplitude of external excitation force on the system's response

After changing the amplitude of the external excitation force  $F_t$ , the bifurcation diagrams of the two chaotic paths shown in Figure 10 are obtained.

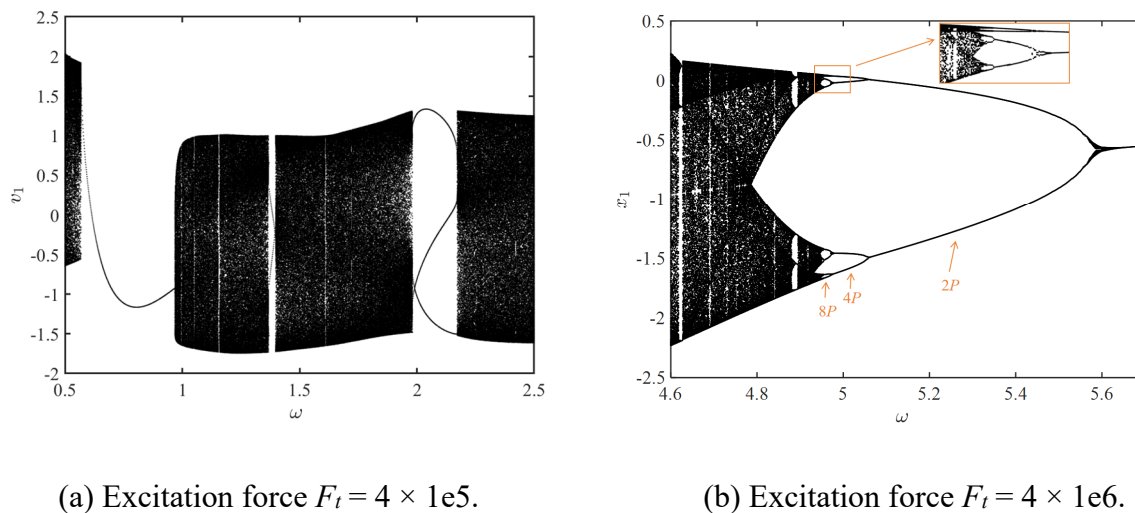


**Figure 10.** Local bifurcation diagrams.

In Figure 10(a), when  $\omega = 0.50$ , the system is quasi-periodic. The bifurcation diagram of the system changes from the oscillation state to the single periodic motion state at  $\omega = 0.535$ , and then at  $\omega = 0.98$ , the system enters the phase-locked oscillation state with a rational multiple of the external

excitation period. The phase diagram of the system is shown as a quasi-periodic oscillation state in Figure 11(d). When  $\omega \in [1.384, 2.5]$ , it is also a period-doubling and phase-locked oscillation state, and the Poincaré maps are shown in Figure 11(e)–(h).

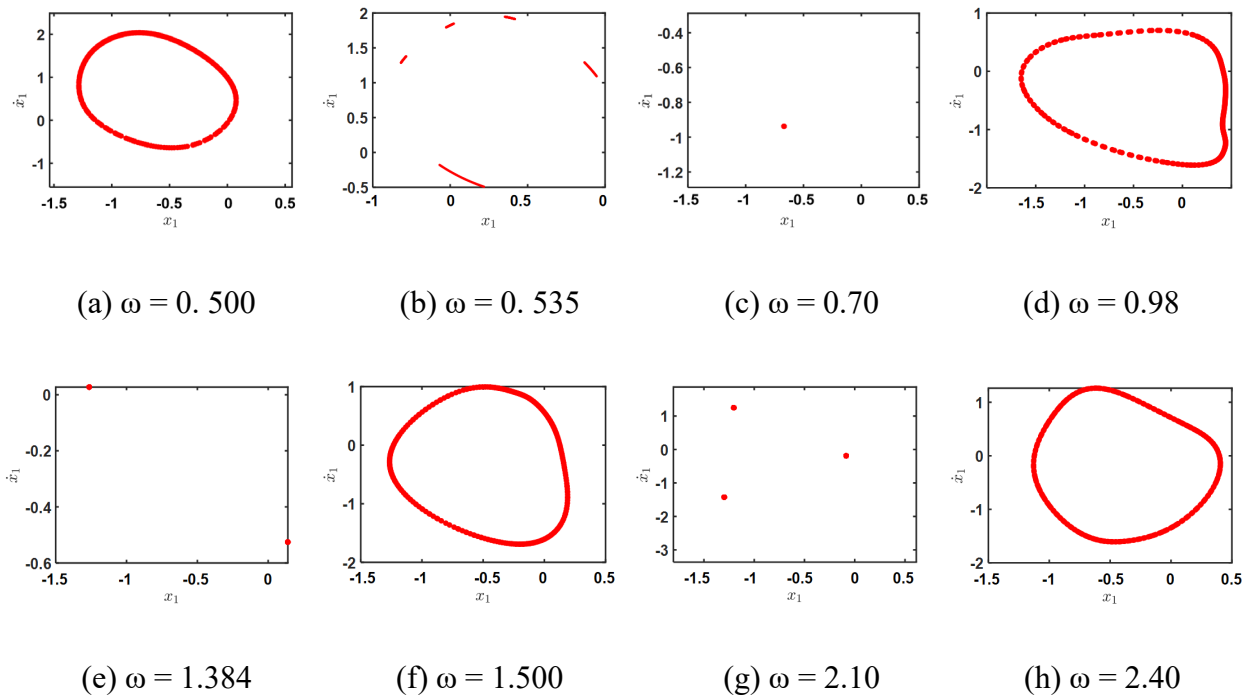


**Figure 11.** Poincaré maps ( $F_t = 4 \times 1e5$ ).

In Figure 10(b), the classical cascade phenomenon is depicted, which shows successive doubling bifurcation as the external excitation frequency decreases. The system transitions from a single period to multiple periods, and finally to chaos. The Poincaré maps, phase diagrams, and time history diagrams of the system can be seen in Figures 12 to 14.

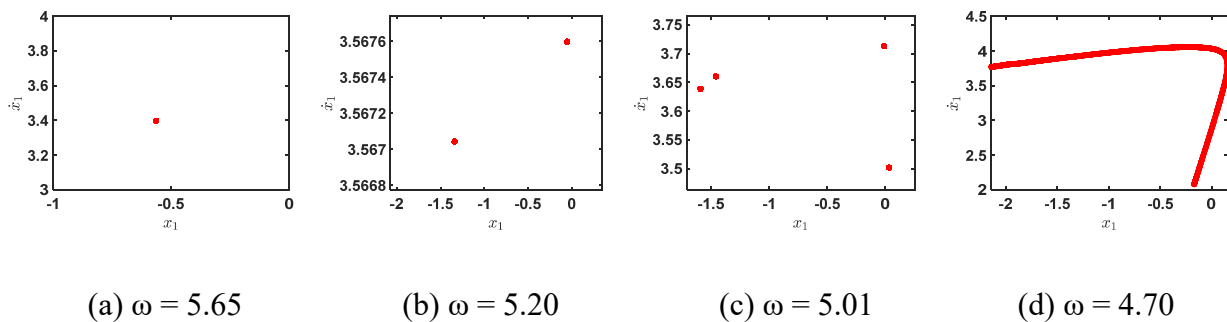


**Figure 12.** Poincaré maps ( $F_t = 4 \times 1e6$ ).

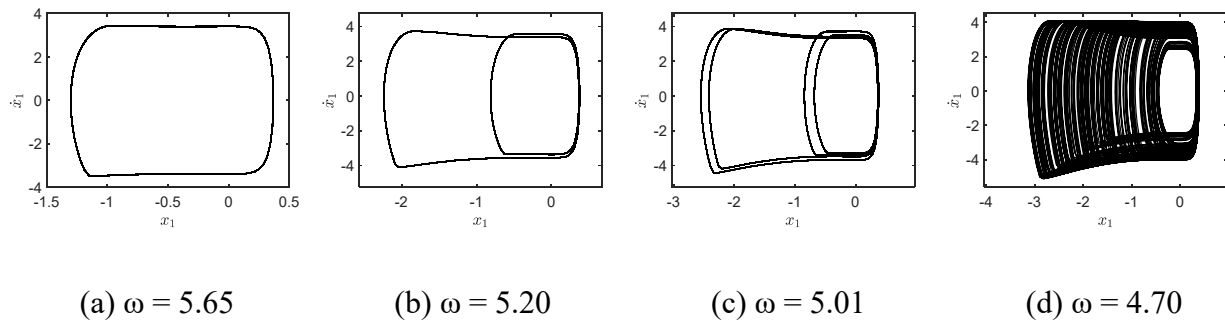


**Figure 13.** Phase plane diagrams ( $F_t = 4 \times 1e6$ ).

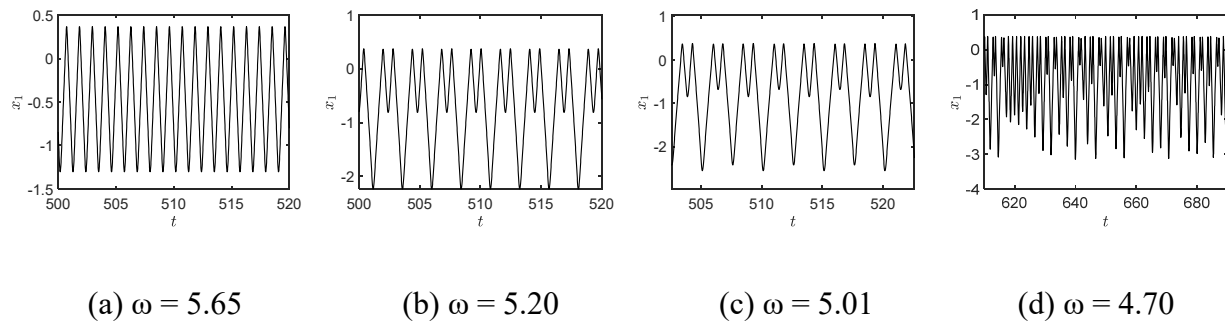


**Figure 14.** Time-domain diagrams ( $F_t = 4 \times 1e6$ ).

### 3.3. The influence of load and damping on the system's response

Keeping the bifurcation parameter  $\omega \in [4, 10]$  unchanged, the numerical simulation analysis of the system was carried out after changing the train's load, and the bifurcation diagrams are shown in Figure 15. In Figure 15, the  $Z$  coordinate axis represents the relative displacement of  $M_L$  when it is impacted during operation, the  $Y$  coordinate axis represents the change in the  $M_L$  load,  $M_v = P \times 10^5$ , and the  $X$  coordinate axis represents the frequency of the external excitation force of  $M_L$ .

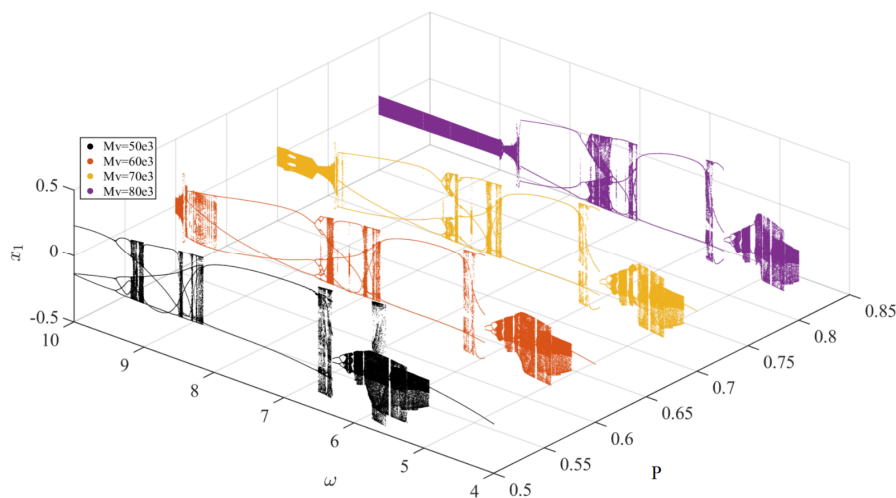


**Figure 15.** Bifurcation diagrams of the system under different loads.

When the train load  $M_v$  is increased and when the external excitation frequency  $\omega = 8.20$ , the system's response gradually shifts from the initial two-period stable motion to the quasi-periodic motion. The Poincaré maps, phase diagrams, and time history diagrams are shown in Figures 16 to 18.

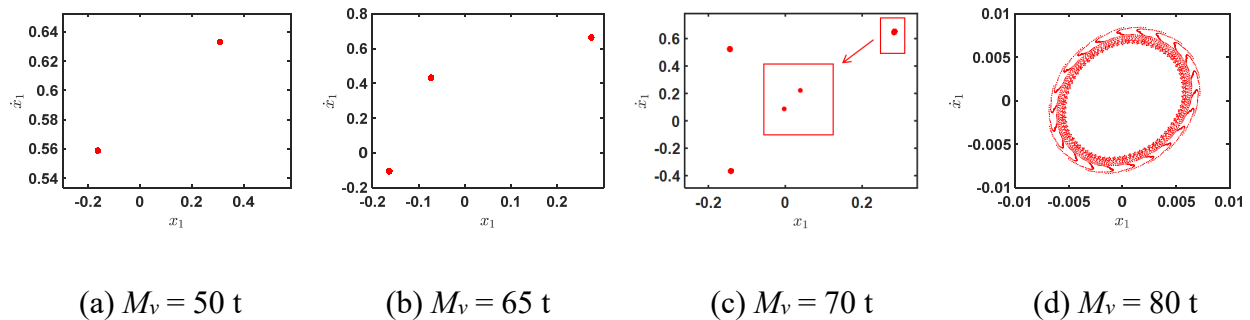


**Figure 16.** Poincaré maps of the system under different loads ( $\omega = 8.20$ ).

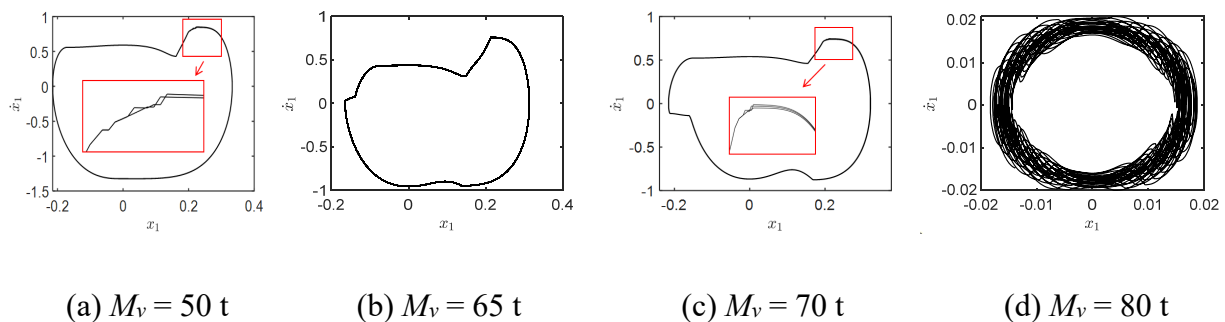


**Figure 17.** The phase diagrams of the system under different loads ( $\omega = 8.20$ ).

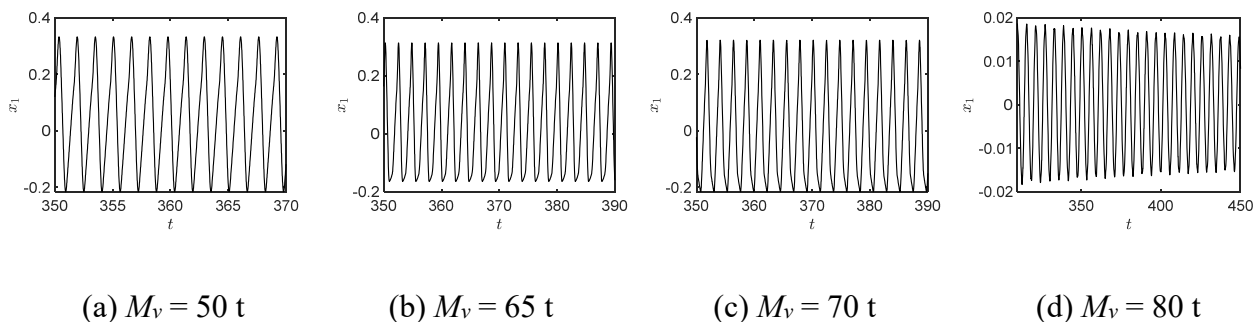


**Figure 18.** The time-domain diagrams of the system under different loads ( $\omega = 8.20$ ).

Keeping the bifurcation parameter  $\omega \in [4, 10]$  unchanged and changing the train damping, the bifurcation diagram of the system is shown in Figure 19. In Figure 19, the  $Z$  coordinate axis represents the relative motion displacement of  $M_L$  when it is impacted during operation, the  $Y$  coordinate axis represents the change in the damping coefficient  $x_{\max}$ , and the  $X$  coordinate axis represents the frequency of external excitation force on  $M_L$ .

Since the damping coefficient  $x_{\max}$  is the denominator of a coefficient of the buffer's mathematical

model, increasing  $x_{\max}$  reduces the system's damping, and then the simulated damping value decreases. A comparison of the system's response when the tuning parameter  $x_{\max}$  increases from 0.2 to 0.35 is shown in Figure 19. When the external excitation frequency  $\omega = 9.0$ , the response of the system changes from three-period stable motion to quasi-periodic motion and finally to chaos. The Poincaré diagrams and time history diagrams are shown in Figures 20 and 21.

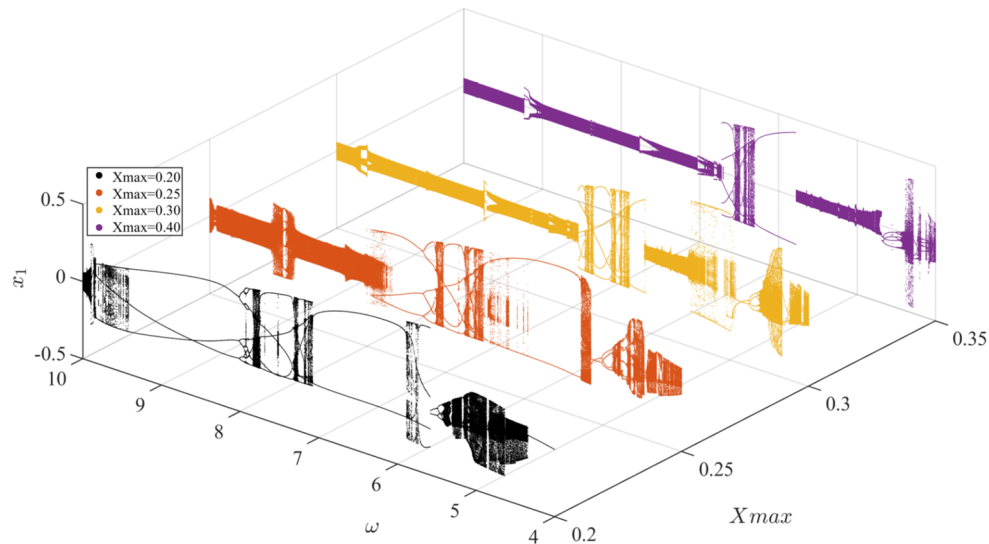


**Figure 19.** Dynamic responses under different levels of damping.

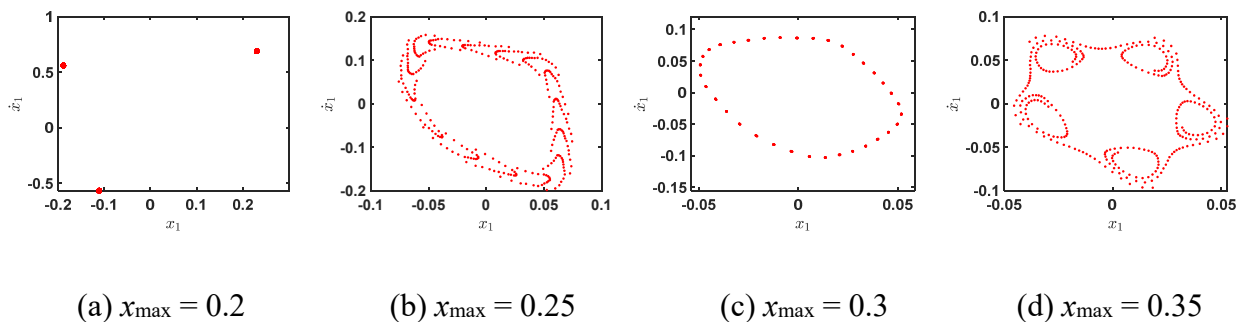


**Figure 20.** Poincaré maps of the system under different levels of damping ( $\omega = 9.0$ ).

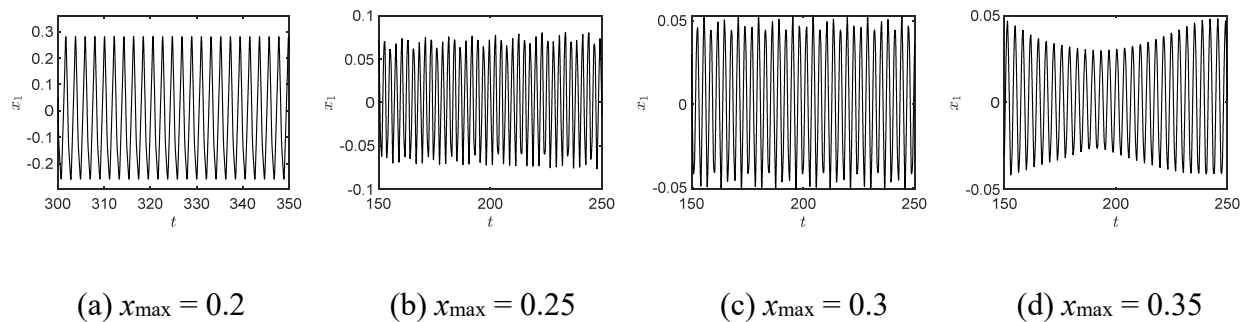


**Figure 21.** Poincaré maps of the system under different levels of damping ( $\omega = 9.0$ ).

By analyzing Figures 15 and 19, it can be found that the system's response changes significantly when the load and damping coefficient are changed. Under the action of different external excitation amplitudes, the system is still dominated by period-doubling bifurcation, but with an increase in  $M_v$ , the bifurcation diagrams show quasi-periodic and saddle-node bifurcation phenomena.

With an increase in the load parameters and a decrease in the damping coefficient, the chaotic region of the system's bifurcation diagrams is obviously expanded. During the actual movement, the long-term operation of the train under these parameters will aggravate the 'slack action' and the longitudinal vibration of the train, so that the components are more likely to age, affecting the safety and stability of the train's operation.

#### 4. Conclusions

In this paper, the mathematical model was established and verified according to the impedance characteristics of the buffer device. By means of numerical analysis, the two-degrees-of-freedom system of a heavy-haul train was studied. Under the change in three states of the external excitation forces, train loads, and the coupler buffer system's performances, the system shows rich nonlinear characteristics such as period-doubling bifurcation, quasi-periodic, phase-locked oscillation, and chaos.

The amplitude of the external excitation force  $F_p$  will change the path of the system entering the chaotic state. Excessive load and reduced damping performance will lead to the expansion of the chaotic region. Selecting the appropriate load and appropriate capacity of the buffer to make the train avoid the chaotic region is conducive to the safety and stability of the train's operation. By studying the bifurcation characteristics and chaos of the system, according to the set characteristics of the attractor, engineers can be assisted in diagnosing faults in the vehicle in time to prevent accidents.

#### Use of AI tools declaration

The authors declare they have not used artificial intelligence (AI) tools in the creation of this article.

#### Acknowledgments

This work was supported by the Special Funds for Guiding Local Scientific and Technological Development by the Central Government of China (22ZY1QA005). The authors are grateful for the financial support. The authors would also like to thank the editor and reviewers for their valuable comments. Finally, we would like to thank Dr. Jin, who helped with the writing of this paper.

#### Conflict of interest

The authors declare there is no conflict of interest.

## References

1. O. P. Yadav, N. S. Vyas, Influence of slack of automatic AAR couplers on longitudinal dynamics and jerk behavior of rail vehicles, *Veh. Syst. Dyn.*, **61** (2023), 2317–2337. <https://doi.org/10.1080/00423114.2022.2107546>
2. C. Feng, Cause analysis and prevention of a series of faults in the lower action coupler-lift rod seat of railway freight cars (in Chinese), *J. Technol. Wind*, **19** (2021), 187–189. <https://doi.org/10.19392/j.cnki.1671-7341.202119084>
3. S. Zhao, Failure analysis and solutions of coupler buffer device of railway freight car (in Chinese), *Harbin Railway Technol.*, **04** (2020), 7–8+32.
4. J. Wang, C. Gong, Analysis and treatment of common faults of coupler buffer device for railway freight cars (in Chinese), *J. Technol. Wind*, **20** (2019), 174–175. <https://doi.org/10.19392/j.cnki.1671-7341.201920149>
5. J. Xu, T. Zhu, M. Yin, C. Wang, S. Xiao, G. Yang, et al., An analytical method for coupler strength of heavy-haul trucks (in Chinese), *Mach. Build. Autom.*, **51** (2022), 29–33. <https://doi.org/10.19344/j.cnki.issn1671-5276.2022.02.009>
6. P. Li, T. Zhu, C. Wang, S. Xiao, Nonlinear finite element simulation analysis of coupler strength of heavy haul trucks (in Chinese), *Mach. Build. Autom.*, **50** (2021), 90–94. <https://doi.org/10.19344/j.cnki.issn1671-5276.2021.03.023>
7. T. Qin, X. Ren, F. Hu, Y. Liu, N. Ao, Q. Kan, et al., Residual life prediction of coupler yoke of heavy haul railway freight car based on measured load spectrum (in Chinese), *Chin. J. Theor. Appl. Mech.*, **54** (2022), 1830–1838.
8. X. Tian, T. Zhu, C. Wang, M. Yin, J. Xu, S. Shou, et al., Research on fatigue life of coupler knuckle of railway heavy haul freight car based on equivalent crack method (in Chinese), *J. Mech. Strength*, **44** (2022), 696–704. <https://doi.org/10.16579/j.issn.1001.9669.2022.03.026>
9. M. Yin, *Research on Data-Driven Prediction Method of Full Life and Residual Life of Freight Car Couplers (in Chinese)*, Master thesis, Southwest Jiaotong University, 2021. <https://doi.org/10.27414/d.cnki.gxnju.2021.002143>
10. H. Yang, J. Yuan, Y. Fu, Z. Li, Dynamic characteristics of heavy haul train QKX100 and MT-2 buffer (in Chinese), *J. Beijing Univ. Technol.*, **46** (2020), 1018–1026.
11. X. Zhao, *Research on Dynamic Model of HM-1 Buffer Based on Impact Test (in Chinese)*, Master thesis, Dalian Jiaotong University, 2018.
12. X. Wang, *Research on the Modeling of MT-2 Buffer with Compression Speed Characteristics (in Chinese)*, Master thesis, Dalian Jiaotong University, 2023.
13. W. Wei, Y. Hu, Q. Wu, X. Zhao, J. Zhang, Y. Zhang, An air brake model for longitudinal train dynamics studies, *Veh. Syst. Dyn.*, **55** (2017), 517–533. <https://doi.org/10.1080/00423114.2016.1254261>
14. O. P. Yadav, N. S. Vyas, The influence of AAR coupler features on estimation of in-train forces, *Railway Eng. Sci.*, **31** (2023), 233–251. <https://doi.org/10.1007/S40534-022-00297-8>
15. T. Zhu, J. Zhang, Q. Wu, R. Lv, X. Wang, S. Xiao, et al., Review of the influence of coupler buffer device on the collision safety of rail train (in Chinese), *J. Traffic Transp. Eng.*, **21** (2021), 233–249. <https://doi.org/10.19818/j.cnki.1671-1637.2021.01.011>
16. C. Yang, Q. Li, X. Wang, Application of generalized multi-step explicit integration algorithm for nonlinear rail vehicle dynamics (in Chinese), *J. Dyn. Control*, **18** (2020), 51–55.

17. Z. Zhang, G. Li, G. Chu, H. Zu, D. Kennedy, Compressed stability analysis of the coupler and buffer system of heavy-haul locomotives, *Veh. Syst. Dyn.*, **53** (2015), 833–855. <https://doi.org/10.1080/00423114.2015.1023318>
18. J. Liu, *Research on the Influence of Buffer Modeling on Train Longitudinal Dynamics Simulation (in Chinese)*, Master thesis, Southwest Jiaotong University, 2019. <https://doi.org/10.27414/d.cnki.gxnju.2019.001564>
19. L. Yang, S. Luo, M. Fu, W. Zeng, Numerical simulation of impedance characteristics of friction buffer in service (in Chinese), *J. China Railway Soc.*, **46** (2024), 57–65.
20. E. D. Ward, R. G. Leonard, Automatic parameter identification applied to a railroad car dynamic draft gear model, *J. Dyn. Syst. Meas. Control*, **96** (1974), 460–465. <https://doi.org/10.1115/1.3426846>
21. Z. Zhang, K. Lv, G. Chu, H. Qi, F. Wang, Research on dynamic simulation method and dynamic performance of 102 type coupler and draft gear for heavy haul locomotive (in Chinese), *J. Vibr. Shock*, **43** (2024), 12–21+59. <https://doi.org/10.13465/j.cnki.jvs.2024.02.002>
22. Q. Wu, S. Luo, Z. Xu, W. Ma, Coupler jackknifing and derailments of locomotives on tangent track, *Veh. Syst. Dyn.*, **51** (2013), 1784–1800. <https://doi.org/10.1080/00423114.2013.830184>
23. J. Duan, W. Zhou, D. Li, C. Grebogi, Birth of strange nonchaotic attractors in a piecewise linear oscillator, *Chaos*, **32** (2022), 103106. <https://doi.org/10.1063/5.0096959>
24. Z. Wei, Y. Li, T. Kapitaniak, W. Zhang, Analysis of chaos and capsizing of a class of nonlinear ship rolling systems under excitation of random waves, *Chaos*, **34** (2024), 043106. <https://doi.org/10.1063/5.0187362>
25. K. Popp, P. Stelter, Stick–slip vibrations and chaos, *Philos. Trans. R. Soc. London, Ser. A*, **332** (1990), 89–105. <https://doi.org/10.1098/rsta.1990.0102>
26. X. Lv, K. Zhang, X. Zhu, G. Luo, Two-parameter non-smooth bifurcation of a two-degree-of-freedom vibro-impact system, *J. Vib. Eng.*, **36** (2023), 107–115. <https://doi.org/10.16385/j.cnki.issn.1004-4523.2023.01.012>
27. O. P. Yadav, S. R. Balaga, N. S. Vyas, Forced vibrations of a spring–dashpot mechanism with dry friction and backlash, *Int. J. Non-Linear Mech.*, **124** (2020), 103500. <https://doi.org/10.1016/j.ijnonlinmec.2020.103500>
28. O. P. Yadav, N. S. Vyas, Stick–slips and jerks in an SDOF system with dry friction and clearance, *Int. J. Non-Linear Mech.*, **137** (2021), 103790. <https://doi.org/10.1016/j.ijnonlinmec.2021.103790>
29. P. Korondi, J. Halas, K. Samu, A. Bojtos, P. Tamás, *Robot Applications*, BME MOGI, 2014.
30. Q. Wu, M. Spiriyagin, C. Cole, Advanced dynamic modelling for friction draft gears, *Veh. Syst. Dyn.*, **53** (2015), 475–492. <https://doi.org/10.1080/00423114.2014.1002504>
31. T. Hsu, D. A. Peters, A simple dynamic model for simulating draft-gear behavior in rail-car impacts, *J. Eng. Ind.*, **100** (1978), 492–496. <https://doi.org/10.1115/1.3439467>
32. C. Cole, M. Spiriyagin, Q. Wu, C. Bosomworth, Practical modelling and simulation of polymer draft gear connections, in *First International Conference on Rail Transportation 2017*, American Society of Civil Engineers, (2018), 413–423. <https://doi.org/10.1061/9780784481257.041>
33. Z. Fu, *Research on the Dynamic Model of MT-2 Buffer Based on Impact Test (in Chinese)*, Master thesis, Dalian Jiaotong University, 2018.
34. Y. Chu, Y. Chang, J. Zhang, *Numerical Calculation Method (in Chinese)*, Science Press, 2016.

- 
35. G. Luo, J. Xie, *Periodic Motion and Bifurcation of Vibro-Impact System (in Chinese)*, Science Press, 2004.
  36. B. Liu, J. Peng, *Nonlinear Dynamics (in Chinese)*, Higher Education Press, 2004.



AIMS Press

©2025 the Author(s), licensee AIMS Press. This is an open access article distributed under the terms of the Creative Commons Attribution License (<http://creativecommons.org/licenses/by/4.0>)